ISSN 1392-3730/eISSN 1822-3605

VILNIUS TECH
Vilnius Gediminas Technical University

JOURNAL of CIVIL ENGINEERING and MANAGEMENT

2025
Volume 30
Issue 1
Pages 52–70
https://doi.org/10.3846/jcem.2024.22266

ELECTROMAGNETIC WAVE-DRIVEN DEEP LEARNING FOR STRUCTURAL EVALUATION OF REINFORCED CONCRETE STRENGTH

Alan PUTRANTO[1], Bo-Xun HUANG[2], Tzu-Hsuan LIN[2]✉

[1] *Department of Civil Engineering, Ketapang State Polytechnic, Ketapang, Indonesia*
[2] *Department of Civil Engineering, National Central University, Taoyuan, Taiwan*

Article History:
- received 9 October 2023
- accepted 27 July 2024
- first published online 5 November 2024

Abstract. Monitoring the performance of reinforced concrete structures, particularly in terms of strength reduction, presents significant challenges due to the practical limitations of traditional detection methods. This study introduces an innovative framework that incorporates a non-destructive technique using electromagnetic waves (EM-waves) transmitted via Radio Frequency Identification (RFID) technology, combined with two-dimensional (2-D) Fourier transform, fractal dimension analysis, and deep learning techniques to predict reductions in structural strength. Experiments were conducted on three reinforced concrete beam (RCB) specimens exhibiting various levels of reinforcement corrosion. From these, a dataset of 1,800 EM-wave images was generated and classified into "normal" and "reduced strength" categories. These categories were used to train and validate a Convolutional Neural Network (CNN), which demonstrated robust performance, achieving a high accuracy of 0.91 and an F1-score of 0.93 in classifying instances of reduced structural strength. This approach offers a promising solution for detecting strength reduction in reinforced concrete infrastructures, enhancing both safety and maintenance efficiency.

Keywords: Convolutional Neural Network (CNN), electromagnetic waves, fractal dimension analysis, radio frequency identification (RFID), strength reduction detection.

✉Corresponding author. E-mail: ***cornetlin@gmail.com***

1. Introduction

Reinforced Concrete (RC) structures are foundational to modern infrastructure. It faces a persistent challenge from corrosion, a pervasive issue with significant economic and safety implications. A study has estimated that the direct economic impact of corrosion, focusing solely on highway bridges, amounts to an astonishing US$ 13.6 billion, with indirect costs potentially escalating up to ten times this figure (Fan & Shi, 2022). Although these structures are designed with a predetermined service lifespan, the insidious progression of corrosion can lead to significant degradation, thereby altering the structural behavior well within its expected service life (Mehta & Monteiro, 2014). In severe cases, corrosion can cause sudden failures, especially in the absence of regular inspections and timely maintenance measures (Taiwan Transportation Safety Board, 2020). Therefore, it is essential to preemptively identify and comprehend the failure mechanisms in RC structures to mitigate catastrophic outcomes and prevent economic losses.

Previous investigations into corrosion-induced failure mechanisms in RC structures have yielded notable findings. Empirical tests, alongside finite element models, demonstrate that reinforcement corrosion in RC structures compromises ductility and alters failure modes under various loading conditions (Ramesht, 1995; Ballim et al., 2001; Ballim & Reid, 2003; El Maaddawy et al., 2005; Val, 2007; Du et al., 2007; Zhu et al., 2013; Zhang et al., 2018; Li et al., 2022). Although specific model guidelines for corrosion assessment have been developed, they highlight the inherent challenges in obtaining reliable field data (Coronelli & Gambarova, 2004). Non-destructive testing (NDT) methods have gained researchers attention as viable techniques for damage assessment (Taheri, 2019; Senin et al., 2019; Rucka & Wilde, 2015; Behnia et al., 2014), with technologies utilizing electromagnetic waves (EM waves) and acoustic emissions being particularly effective for corrosion detection (Li et al., 2021). Radiofrequency Identification (RFID) leveraging EM waves has emerged as a promising NDT method. RFID technology is highly adaptable, cost-effectiveness, and low maintenance requirements (Meng & Li, 2016; Zhang et al., 2017). The interaction of EM waves between RFID reader and sensor tags in RC structures has been extensively studied (Halabe et al., 1989; Chiba & Miyazaki, 1998; Jiang & Georgakopoulos, 2011; Jiang et al., 2012), and the integration of embedded sensors leveraging RFID for damage diagnosis in RC structures remains a dynamic research area (Bartholmai et al., 2016; Strangfeld et al., 2019; Lin et al., 2021, 2022; Ferreira et al., 2022). Despite these foundational researches, there is an immediate need for more adaptable approach to enhance decision-making related to the assessment of reduction strength in RC structures. Traditional methodologies for evaluating RC structural performance often require extensive analytical expertise and are labor-intensive (Azad et al., 2007; Jnaid & Aboutaha, 2016; Campione et al., 2017; Fernandez et al., 2018; Chalioris et al., 2021).

In recent years, machine learning and deep learning techniques have emerged as powerful tools for assessing civil infrastructures (Zhang et al., 2023; Nguyen & Chou, 2024; Obunguta et al., 2024; Tao & Xue, 2024; Lin et al., 2024a). These techniques leverage large datasets to train models capable of detecting and classifying defects with high accuracy (Lin et al., 2024b). Convolutional Neural Networks (CNNs) have been extensively used for image-based inspection, detecting cracks, spalling, and other surface defects. Cha et al. (2017) and Laxman et al. (2023) developed a CNN-based framework for crack detection in concrete structures, which demonstrated high accuracy in distinguishing cracks defect. Yeum and Dyke (2015) utilized CNNs to detect spalling and other surface anomalies, achieving high detection rates even in complex environments. Additionally, Dogan et al. (2023) employed deep transfer learning algorithm to distinguish between earthquake-induced and corrosion-related damages in reinforced concrete buildings in earthquake-prone regions. Atha and Jahanshahi (2018) explored CNN for autonomous corrosion detection, which can reduce inspection time and increase objectivity, while, Cavaleri et al. (2022) developed convolution-based ensemble learning models to estimate the bond strength of the corroded reinforced concrete. Most studies utilizing CNNs have been assessing local defects in reinforced concrete structures. Despite the significant progress in utilizing deep learning techniques for RC assessment, their application in predicting concrete strength reduction for overall structural performance due to corrosion has not been extensively explored. This gap presents a unique opportunity to advance the capabilities of structural health monitoring systems. The use of CNNs to predict and classify strength reduction could provide more comprehensive insights into the structural integrity of RC structures, thus offering a more robust tool for maintenance planning and risk mitigation. By leveraging CNNs to extend beyond local defect detection, this study aims to develop a holistic approach to assess the overall performance of RC structures, incorporating advanced image processing and deep learning technique to offer precise evaluations.

This research investigates and develops an advanced methodology that integrates EM waves through RFID technology with image processing and deep learning techniques to assess the reduction in structural strength of reinforced concrete structures. Our approach combines the principles of two-dimensional (2D) Fourier transforms with the complex concepts of fractal dimensions and deep learning model prediction, enabling a comprehensive assessment of the overall performance of RC structures. To validate our proposed method, we constructed three RC beam specimens with varying levels of reinforcement corrosion.

2. Method

2.1. Overview of reinforced concrete strength assessment with EM-wave and deep learning technique

In this study, we investigated the reduction in strength of reinforced concrete structures due to the effects of corrosion. Three RC beam specimens with varying levels of pitting corrosion were constructed. The pitting corrosion was introduced and controlled manually by reducing the cross-section and the weight of reinforcement at designated locations using a grinder. Several static loading mechanisms were designed to observe and measure crack propagation and sensor responses. The loading and sensor response measurements continued until the RC beam specimens reached their maximum loading capacity or failure.

The sensor response data (frequency data in kHz) were then analyzed using image processing techniques to build an image dataset, a process we define as encoding images. Once all the sensor data from the RC specimens were converted to an encoded image dataset, the dataset was further processed and analyzed using the open-source software Gwyddion. This transformation involved applying 2D Fast Fourier Transforms (2D-FFT) (Draudvilienė et al., 2022) and the Otsu method to visualize the sensor responses relative to the specimens' physical conditions. We utilized fractal dimension analysis to measure image complexity at different scales, which served as an indicator of the reduction in strength for subsequent deep learning model predictions. Given the small image dataset and to mitigate potential overfitting in the model predictions, we employed K-fold cross-validation for our Convolutional Neural Network model in predicting and classifying RC conditions. The technical roadmap of the proposed framework is illustrated in Figure 1. Our dataset and the associated code can be accessed at https://zenodo.org/records/12671514.

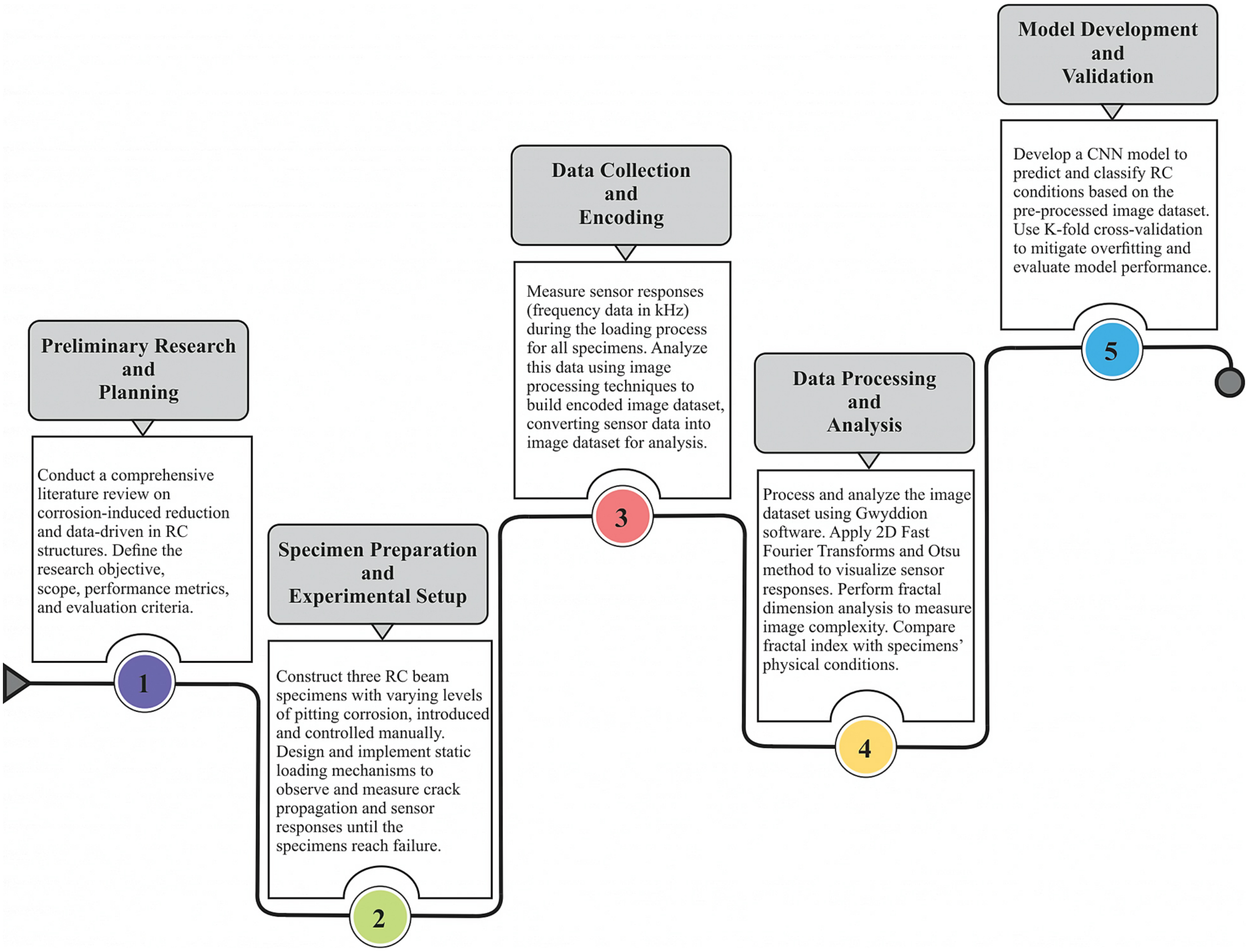

Figure 1. Technical roadmap of the proposed framework for evaluating strength reduction in reinforced concrete structures

2.2. Ultra-high frequency radio-frequency identification system

In this study, we developed and implemented an ultra-high frequency (UHF) radio-frequency identification (RFID)-based system to detect structural damage. The system leverages the wireless communication properties inherent to RFID technology to facilitate continuous structural health monitoring. The RFID system, designed with practicality in mind, is composed of several key components: RFID tags, readers, antennas, and an advanced data processing unit. These tags are strategically affixed at crucial locations within the structure, enabling the system to detect changes indicative of damage to RC specimens. The data corresponding to these sensed parameters are then transmitted to the RFID readers via antennas, providing real-time information for structural health monitoring.

Figure 2 illustrates the overall RFID system, in which, Figure 2a presents an overview of the sensing mechanism, which integrates an RFID reader, a user interface, and advanced smart tags. The tag, detailed in Figure 2b, consists of an antenna coupled with a self-tuning sensor-code integrated circuit (IC). This IC, which is the core of the tags, can adjust to 32 different capacitance states, each represented by a 5-bit sensor code. This allows the device to capture and convert specimen change indicators into digital signals. The antenna's main role is to send these signals back to the RFID reader. The Electronic Product Code (EPC) is embedded within most smart sensor tags, which uniquely identifies each physical object. The tags detect analog signals, including Received Signal Strength Indicator (RSSI), frequency, and sensor-code value, which the self-tuning IC then digitizes. The RSSI explicitly measures the strength of the signal that the smart sensor tag sends back to the RFID reader after an electromagnetic wave traverses the path from the reader to the tag. The RC beam test during the loading mechanism captured by these parameters is displayed on a computer terminal user interface, as shown in Figure 2c. In RFID systems that utilize such sensing mechanisms, employing smart sensor tags with integrated single-chip ICs simplifies deployment and eliminates the need for maintenance or batteries. The RFID system operates in a frequency range of 902000–928000 kHz. Each oblong-shaped tag, measuring 101.7 mm by 31.9 mm, is composed of three layers: an upper antenna assembly extending towards both ends and covered with paper, a central layer housing the IC and sensing mechanism, and a self-adhesive base that facilitates attachment to diverse materials. Although these sensor tags are designed to adapt to various environmental conditions, the specific properties of concrete may lead to detuning, potentially compromising their functionality.

Additionally, compression tests posed a risk of damaging the embedded tags. Thus, we developed a protective tag casing using 3D printing technology, as depicted in Figure 2d. This casing, made of 3D-printed plastic, was designed with a focus on protection and adaptability. It safeguards the tags from environmental factors and potential damage and ensures their optimal performance in various structural settings, thus enhancing the system's reliability and longevity.

2.3. Data processing

In our study, we utilized the frequency parameter as an indicator of structural integrity for individual segments of reinforced concrete beams. To assess the overall condition of these structures, we employed convolutional neural network models in conjunction with a novel image processing technique. This dataset construction involved encoding frequency data obtained from RFID readings. Sensor data for each RCB segment were collected under normal conditions (for specimens without introduced pitting) and under conditions of reduced strength (for specimens with pitting corrosion on their reinforcement), and initially captured in CSV file format. The frequency data, denoted as ai,j, is located at the i-th row and the j-th segment of the RCB specimen in the spreadsheet, as depicted in Figure 3. Following data collection, we executed preprocessing procedures, including data normalization, to ensure uniformity and enhance data quality. The processed data were subsequently formatted to support grayscale and depth representations, facilitating image reconstruction, and a custom-encoded program used for dataset construction is detailed in Appendix.

Figure 3 illustrates the image reconstruction process, which was conducted using Python and leverages well-known libraries such as NumPy for data manipulation, Pandas and the Python Imaging Library (PIL) for image processing tasks, and Matplotlib for visualization purposes. To increase the informational value of the images, specific post-processing methods were implemented. During the preprocessing stage, frequency data encoding thresholds were set from 902000 to 928000 kHz. These values were then standardized to align with an 8-bit grayscale format, where each pixel's intensity is represented across a

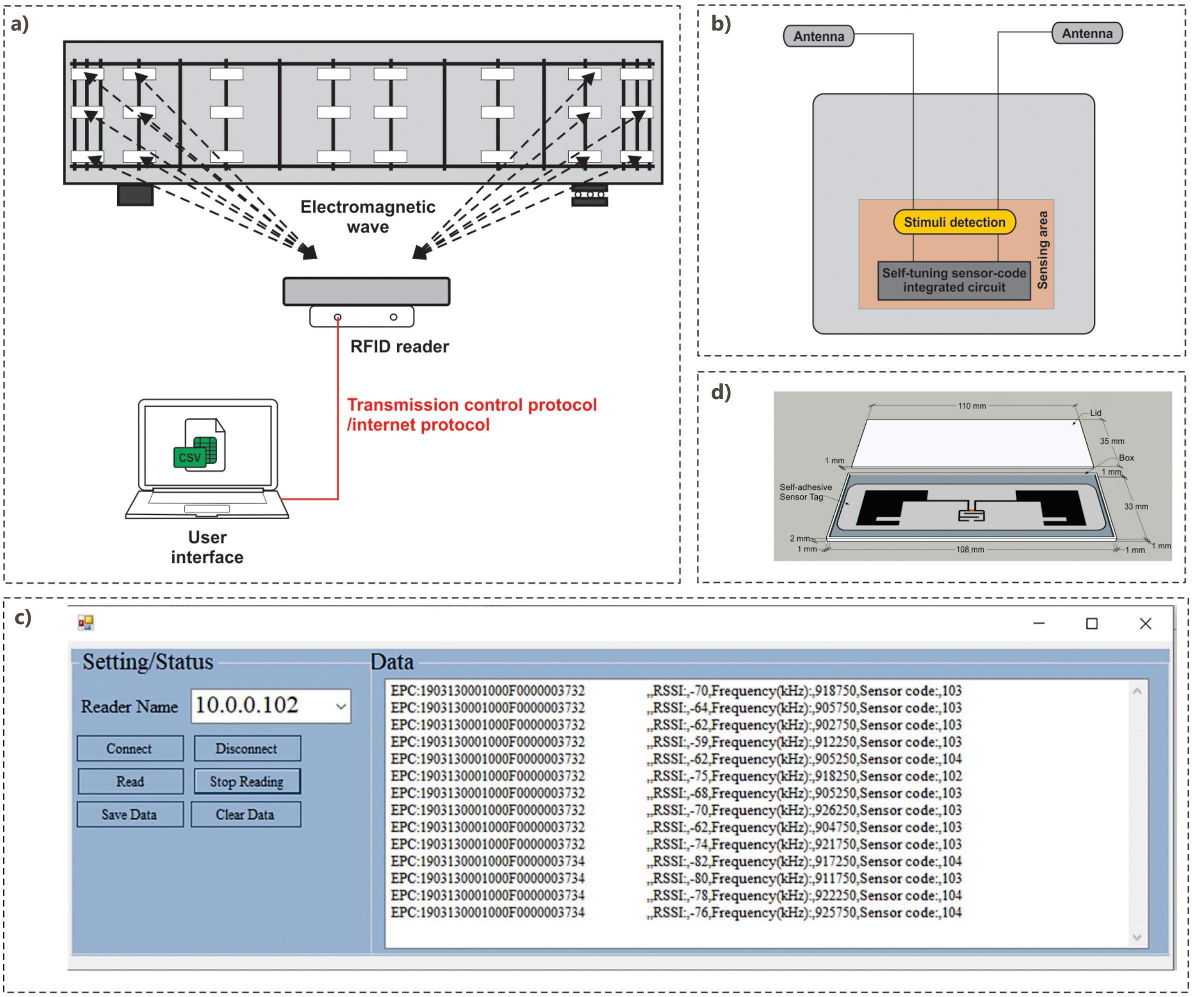

Figure 2. RFID system for a – the overall sensing mechanism; b – RFID tag component; c – user interface; d – 3D-printed case for embedding applications

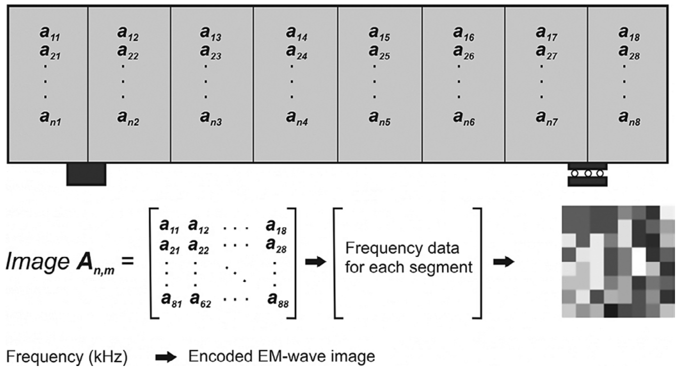

Figure 3. Dataset construction

spectrum of 256 shades of gray. Following this, our image dataset underwent a transformation to a 16-bit grayscale format via advanced image processing techniques. The decision to use a reduced bit depth in the images was made to improve computational efficiency and memory utilization, which in turn facilitates faster model training and improved convergence rates (Putranto et al., 2024). Additionally, this study focused on extracting critical features pertaining to the texture and shape influenced by electromagnetic waves images, which are essential for the image classification.

To improve encoded image interpretation, we applied image transformation techniques to convert a two-dimensional (2D) data array from the spatial domain to the more informative frequency domain (Putranto et al., 2023). This transformation was facilitated by using the 2D-FFT, a robust algorithm designed to efficiently compute an image's discrete Fourier transform (DFT). The FFT substantially reduces the computational burden associated with DFT calculations, decreasing the complexity from O(N2) to O(NlogN), where N represents the number of data points in the image. This enhancement is vital for managing the large volumes of data typical in image processing tasks. The mathematical principles underlying this transformation for an image matrix of size $M \times N$ (Gonzalez & Woods, 2018), denoted as $f(x, y)$, are shown below:

$$F(u,v) = \sum_{x=0}^{M-1} \sum_{y=0}^{N-1} f(x,y) \cdot e^{-j2\pi\left(\frac{ux}{M} + \frac{vy}{N}\right)}. \quad (1)$$

In this context, $F(u, v)$ denotes the image in the frequency domain, while $f(x, y)$ represents the original image in the spatial domain. The variables M and N correspond to the image's height and width, respectively. The spatial frequencies u and v are essential for analyzing the content of the frequencies and are aligned with the x and y axes, respectively. The symbol j represents the imaginary unit, crucial for expressing complex numbers that capture both the phase and magnitude of the frequency components. In subsequent, we utilize Otsu's method for image segmentation and then compute the fractal dimension (D). To extract valuable insights from the encoded image, a 2D-FFT was applied employing Hamming windowing. A pre-processing step was necessary that involving the separation of low and high frequencies within the encoded image. This separation was achieved by implementing a low-pass filter on the transformed encoded image, followed by the segregation of intensity bins utilizing Otsu's segmentation method. In the subsequent analysis, the fractal dimension was employed as a metric to assess the transformed encoded image's characteristics. We utilize fractal dimension to quantify the complexity of the texture and structural details within the images' dataset.

The concept of the fractal dimension has been extensively employed to discern complex patterns inherent in images through image processing techniques. The fractal dimension stands as a pivotal metric, offering insights into the intricacies and irregularities that typify numerous physical and engineering systems. It essentially quantifies the proportionality between the intricacy of a pattern and the scale at which it's observed. Our study utilizing box counting method to calculate fractal dimension. This technique entails superimposing a grid on the object of interest and enumerating the grid boxes that encapsulate the structure, observed across varying scales. The relationship between the logarithm of the count of boxes, N, and the logarithm of the reciprocal scale, h, serves to approximate the fractal dimension, as expressed by:

$$D = \frac{\log(N)}{\log(h)}. \quad (2)$$

The image preprocessing technique applied to the initial image dataset (shown in Figure 4a) included 2D FFT (with results shown in Figure 4b), Otsu's segmentation (with results shown in Figure 4c), and the calculation of the fractal dimension for each image. These processes were conducted using the open-source software Gwyddion to prepare the dataset for the CNN model.

2.4. Deep learning model prediction with Convolutional neural network

In this research, we utilized Convolutional Neural Networks (CNNs) to analyze and classify images derived from electromagnetic wave readings of reinforced concrete conditions. CNNs are particularly suited for processing data arranged in grid-like structures, such as image pixels, due to their ability to autonomously extract and hierarchically organize features from raw images. This capability begins at

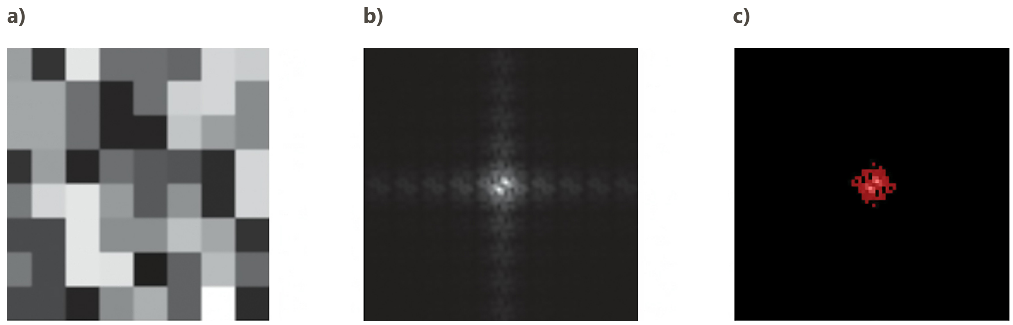

Figure 4. Image data representation: a – encoded image with $n \times n$ pixels, illustrating the initial data format; b – frequency domain representation of the image; c – thresholded image

the initial convolutional layers, where simple features like edges and textures are identified, and progresses through to deeper layers that detect more complex features. Such progressive feature extraction significantly enhances the network ability to interpret visual content, making CNNs an ideal choice for the specific needs of this study.

The architecture of the CNN employed in this study is structured around several key components. It begins with convolutional layers that apply a series of learnable filters to the input images, producing feature maps that highlight essential visual attributes. These layers are followed by ReLU (Rectified Linear Unit) activation functions, which introduce necessary non-linearities that facilitate the learning of complex patterns. Pooling layers subsequently reduce the spatial dimensions of these feature maps, thus decreasing the computational load while simultaneously increasing the robustness of the feature detection process. The culmination of this architecture is seen in the fully connected layers that integrate all previously learned features, leading to a softmax layer that outputs a probabilistic distribution across various classes, thereby enabling effective classification. The detail of CNN model architecture is shown in Figure 5.

To ensure the reliability of our model, we implemented a rigorous preprocessing regimen that standardized images to uniform sizes and formats, which is crucial for consistent processing by the CNN. The network was then trained on a well-annotated dataset using backpropagation and gradient descent algorithms to iteratively minimize classification errors. To robustly evaluate the effectiveness of our model, we employed a K-fold cross-validation technique (with K set to 5), which involved shuffling the dataset (with a set random state of 4 for reproducibility) and dividing it into five subsets. This method allowed each subset to be used for validation once while the others were used for training in each iteration. Such a strategy not only maximized the use of the limited data available but also provided a thorough assessment of the model's predictive accuracy and its ability to generalize across new and unseen data. This comprehensive evaluation is vital for applications in structural integrity assessment, where the accuracy and reliability of the predictive model are paramount.

To classify electromagnetic (EM) wave images of reinforced concrete, we employed a CNN model (see Figure 6). Initially, we collected a dataset comprising 1800 EM-wave images, which were subsequently labeled based on the condition of the concrete: 640 images were categorized as "Normal", and 1260 images were labeled as "Reduced Strength". These images were then divided into training and validation sets, with 70% of the images from

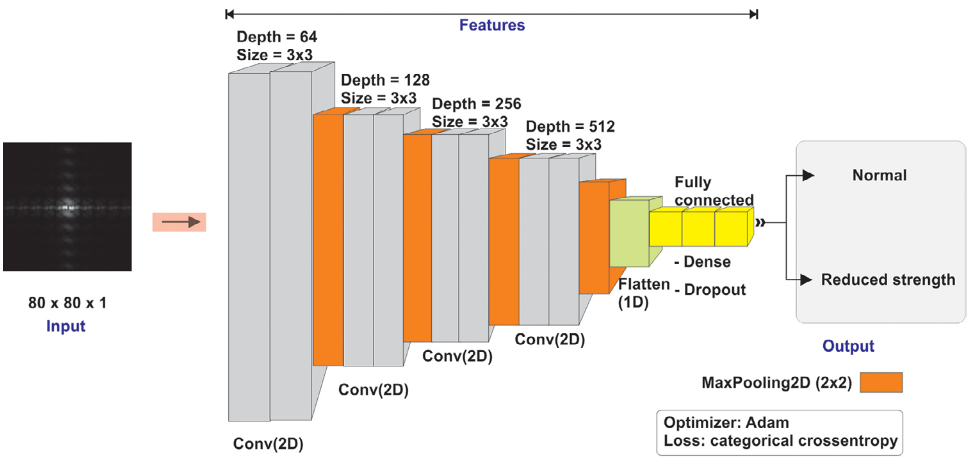

Layer	First	Second	Third	Fourth	Flatten	Dense	Output
Activation	ReLU	ReLU	ReLU	ReLU		ReLU	Softmax

Figure 5. CNN model prediction architecture

each category allocated for training the model and the remaining 30% reserved for validation. Detail of data split for CNN model prediction can be seen in Table 1. The CNN architecture, consisting of multiple convolutional layers, pooling layers, and fully connected layers, was meticulously designed and o0timized for this classification task. Key hyperparameters, including learning rate, batch size, and the number of epochs were fine-tuned to enhance model performance. The training process involved using the training dataset to enable the CNN to learn distinctive features associated with normal and reduced strength concrete. The model's performance was validated using the validation dataset, ensuring its robustness and preventing overfitting. The schematic of training and validation process were shown in Figure 7.

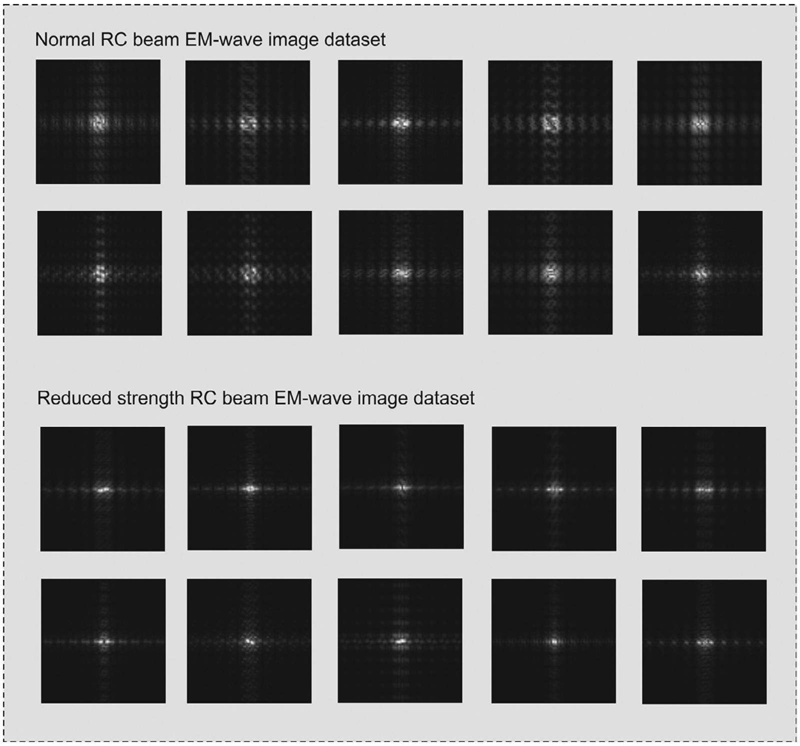

Figure 6. Sample of EM-wave images dataset for training and validation

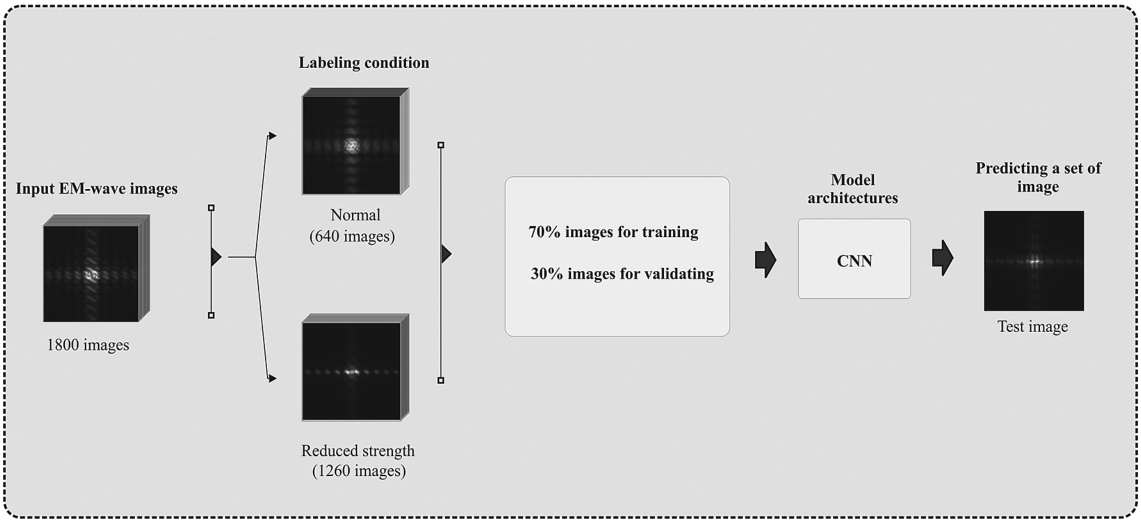

Figure 7. Training and validation process

Table 1. Training and validation split for CNN model

Classification	Training (images)	Validating (images)	Total (images)
Normal	448	192	640
Reduced strength	812	348	1160

3. Experimental design

In this study, we constructed three specimens of reinforced concrete beams (RCBs) to investigate the impact of pitting corrosion on the mechanical performance of reinforced concrete structures. The dimensions of the RCBs were 120 mm × 250 mm × 1500 mm and were cast using a mix proportion of 1:2:3:0.8 (cement: fine aggregate: coarse aggregate: water). The first specimen, hereafter referred as RCB-1, was constructed under normal conditions without artificial pitting on its reinforcement. The second specimen, hereafter referred as RCB-2, was constructed with artificial pitting corrosion on the longitudinal bars. Meanwhile, the third specimen, hereafter referred as RCB-3, was constructed with artificial pitting corrosion on both the transversal and longitudinal bars. The specific locations of the artificial pitting corrosion on the RCB reinforcement can be seen in Figure 8. The severity of corrosion on RCBs are defined as follows: the RCB-1 represented the normal condition with no pitting corrosion present. Next, the RCB-2 is classified as a moderate condition due to the partially corroded on its longitudinal bars. The last is the RCB-3, which represented a severe condition due to corroding on both the transversal and longitudinal bars. The corrosion in this study was evaluated and classified as the wide-shallow pit (ASTM International, 2021).

We meticulously designed an experiment to investigate the impact of pitting corrosion on the structural strength of reinforced concrete beams by simulating realistic corrosion conditions on reinforcement bars. The experiment commenced with a thorough inspection of each steel reinforcement bar, during which pre-determined locations for inducing pitting were systematically marked. These locations were strategically selected along a grid pattern on both longitudinal and transversal reinforcements, emphasizing critical areas such as mid-spans and supports where stress concentrations are typically higher.

The corrosion simulation involved precisely grinding down small sections of the steel bars to reduce their weight by exactly 2.5 grams at each marked location on both the front and back sides of the beam specimen (the front side is shown in Figure 8a. The pitting corrosion details are provided in Figure 8b, where the location (x, y) of (0,0) is defined as the bottom-left side of the beam specimen, followed by specific coordinates of pitting corrosion in the reinforcement framework. This process was rigorously controlled using a precision grinder, ensuring uniformity in the simulation of pitting across all bars. To verify the accuracy of this material removal, the weight of each bar was measured before and after the grinding process using a high-precision digital scale with an accuracy of 0.01 grams. Following the preparation and verification of the reinforcement bars, they were placed in molds corresponding to the dimensions of the designed beams – 120 mm × 250 mm × 1500 mm. These dimensions and the reinforcement layout were chosen to align with standard design practices, ensuring a realistic simulation of field conditions. The concrete mix was then poured into the molds and carefully compacted to eliminate voids and air pockets, forming the beam specimens. Lastly, the experimental procedure was the curing of the concrete beams, which was conducted under standard conditions for 28 days. This duration was critical to achieve optimal strength development in the concrete, ensuring that the beams were adequately prepared for subsequent mechanical loading tests.

Each specimen was embedded with 24 smart sensor tags attached on one side of transversal reinforcement. The smart sensors are grouped into eight sections along the specimen. The smart sensors were protected with the 3D-printed case made from polylactic acid with dimensions 110 mm × 35 mm × 3 mm to prevent sensor damage during the loading phase. The RCB configuration can be seen in Figure 9.

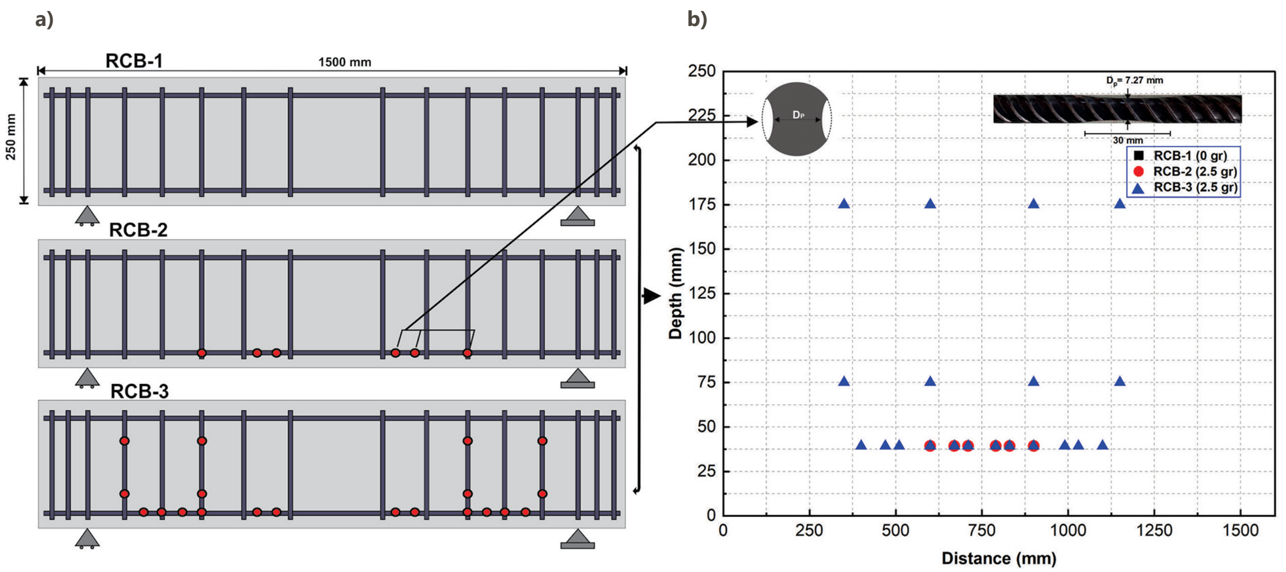

Figure 8. The artificial pitting corrosion: a – displayed on the reinforcement framework; b – detailed location (observed on both sides of the reinforcement framework)

In order to obtain data on reinforced concrete mechanical behavior, the test was set and detailed as follows. First, a wire-strain gauge was attached to each longitudinal bar in the middle section of the RCB, and a linear displacement sensor (LVDT) was used to measure midspan deflection. Next, the radio frequency identification reader is set 50 cm away from the reinforced concrete surface and reads the concrete side attached with smart sensor in sequential (from segment G1 to G8). The EM-wave with radio frequency (902000–908000 kHz) will be transmitted and sent back during measurement time (90 seconds for each group). The frequency measurement was conducted during each loading phase. The overall measurement process can be seen in Figure 10. Last, the cracks on the reinforced concrete surface are measured using a digital microscope for their formation and propagation at post-loading phase.

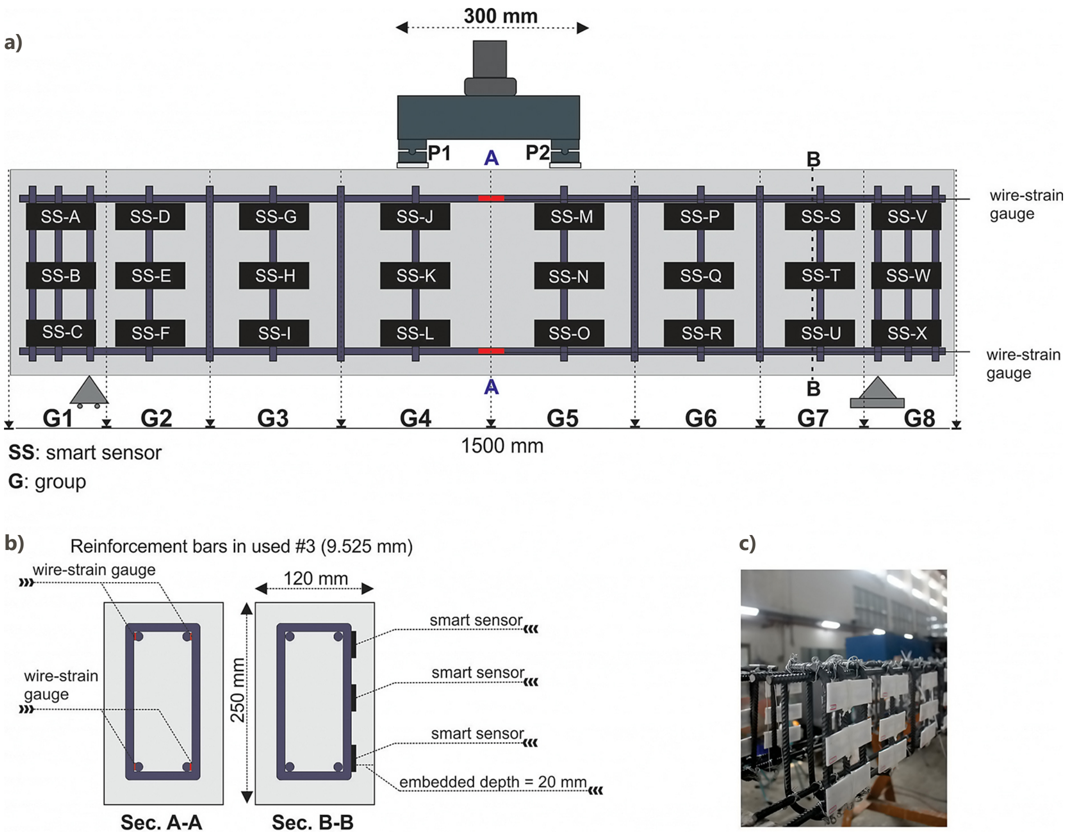

Figure 9. Reinforced concrete beam showing: a – a longitudinal section; b – cross-sections; c – smart sensors on reinforcement bars

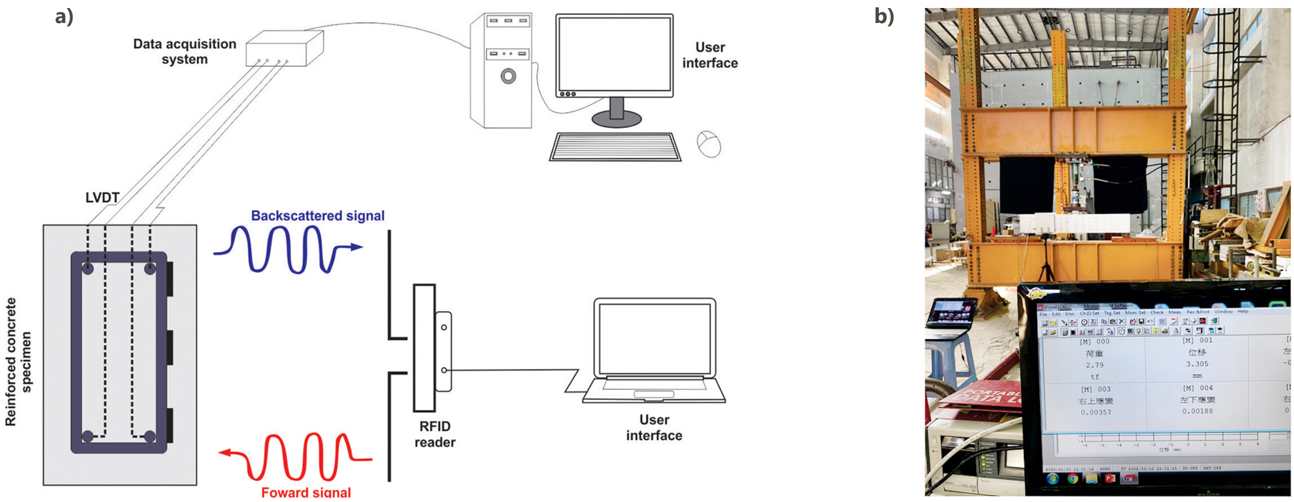

Figure 10. Schematic of the overall experimental architecture

4. Results

4.1. Relation between structural strength and fractal dimension

This study undertook a comprehensive investigation involving the testing of reinforced concrete beam specimens subjected to a series of five distinct loading phases. The load-deflection curves were meticulously analyzed for three specimens exhibiting varying degrees of corrosion, and the findings are thoughtfully presented in Figure 11. The reinforced concrete beams analyzed included RCB-1 (normal condition), RCB-2 (moderate corrosion), and RCB-3 (severe corrosion), with detailed mechanical properties documented in Tables 2, 3, and 4, respectively. Our observations revealed that RCB-1 and RCB-2 exhibited no significant differences in their performance. This similarity can be attributed to the relatively minor degree of corrosion present on the longitudinal reinforcement of RCB-2, which, in turn, exerted only a marginal influence on the overall structural integrity.

For RCB-1, the uncorroded beam, the load-deflection curve demonstrated a typical response with initial flexural cracking occurring at approximately 10 kN, yielding of the reinforcement at around 40 kN, and a maximum load capacity (Pmax) of 58.88 kN. The maximum deflection (δmax) was 14.494 mm. Strain measurements showed minimal initial strains in both the rebar and concrete, with significant increases at higher loads, reflecting the expected progression of cracking and deformation. The crack width analysis revealed a gradual increase in crack width, reflecting typical flexural cracking behavior.

The RCB-2 beam, subjected to moderate corrosion, showed a slight reduction in initial stiffness compared to RCB-1, with flexural cracking occurring at around 9 kN. The beam's load capacity was slightly higher at 59.69 kN, with a δmax of 14.526 mm. Strain data indicated higher initial strain values in both the compression and tension zones, particularly at higher loads, pointing to an earlier onset of yielding and more extensive cracking due to corrosion. However, the overall performance of RCB-2 was not significantly different from RCB-1, attributed to the relatively minor degree of corrosion present on the longitudinal reinforcement, which exerted only a marginal influence on the overall structural strength.

RCB-3, representing severe corrosion, diverged notably from RCB-1 and RCB-2. It exhibited heightened pitting corrosion on both its transverse and longitudinal reinforcement elements, resulting in a significant reduction in stiffness and load capacity. Initial flexural cracking occurred at approximately 8 kN, and the maximum load capacity was reduced to 59.49 kN. The δmax was the highest among the three beams at 15.260 mm, indicating significant deformation. The strain measurements for RCB-3 showed early and substantial increases, particularly in the tension zone, reflecting extensive damage and reduced structural strength. The crack width analysis revealed wider cracks at lower load levels, indicating severe structural distress and potential bond failure between the rebar and concrete.

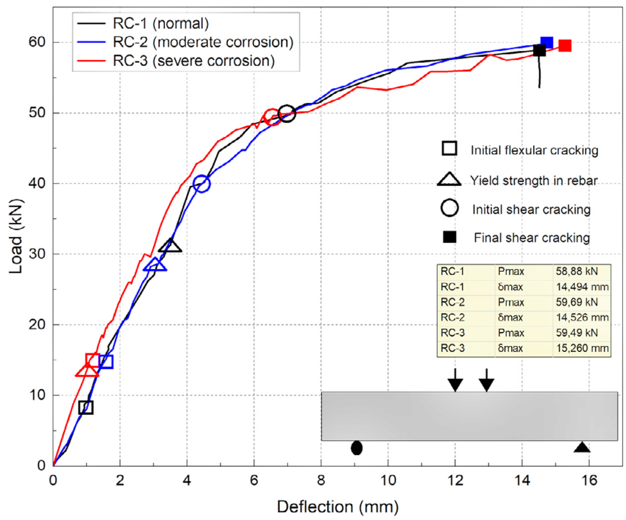

Figure 11. Load-mid span deflection curve

Notably, once RCB-3 surpassed the 85% threshold of the ultimate load, it exhibited a discernible shift towards increased brittleness, marked by the emergence of wider cracks in comparison to RCB-1 and RCB-2. This transition to a more brittle behavior aligns with the findings of Du et al. (2007), highlighting the pivotal role of corrosion in both the tension and compression zones of under-reinforced beams, leading to decreased ductility and a more brittle failure mode.

The results of our study underscore the profound impact of corrosion on the mechanical properties of reinforced concrete beams. When confronted with elevated levels of pitting corrosion affecting both transverse and longitudinal reinforcements, these beams exhibit decreased ductility, eventually culminating in brittle failure as a result of a progressive loading mechanism. This investigation further revealed that the extent of corrosion on the reinforcement significantly influenced the formation of cracks within the reinforced concrete beams. Specifically, the emergence of cracks induced by applied loads was observed to manifest at approximately 25% of the beam's ultimate load when corroded reinforcement was present, whereas the corresponding non-corroded reinforcement exhibited crack formation at approximately 15% of the ultimate load. This observation underscores the profound impact of corrosion on the structural integrity of the beams, with corrosion acting as a pivotal factor in the initiation and progression of cracks.

Moreover, the analysis of maximum deflection in the specimens revealed a distinct pattern. RCB-3 exhibited the highest maximum deflection, followed by RCB-2 and RCB-1, respectively. This pattern of deflection aligns consistently with the degree of corrosion present, with RCB-3 exhibiting the most extensive pitting corrosion on its reinforcement elements. To provide a comprehensive overview of the physical condition of the reinforced concrete beams, detailed information on deflection and mechanical properties is presented in Tables 2 to 4. These tables offer valuable insights into the behavior of the specimens, allowing for a clear comparison of their performance under varying corrosion levels.

In addition, the progression of crack formation in each reinforced concrete beam specimen is visually depicted in Figures 12 through 14. These figures serve as illustrative representations of the profound influence of corrosion on crack initiation and propagation during the loading phase. Specifically, Figures 12a, 13a, and 14a visually capture the crack patterns in RCB-1, RCB-2, and RCB-3 at various load levels, while Figures 12b, 13b, and 14b quantify the load corresponding to each crack width. These figures highlight the load levels at which these cracks occurred, providing a clear correlation between applied load and crack progression. The type of failure observed in the figures for RCB-1, RCB-2, and RCB-3 is predominantly flexural failure. This is indicated by the pattern of vertical and inclined cracks developing primarily at the mid-span region, where the bending moment is highest. The progression and widening of these cracks under increasing loads reflect the beams' flexural response to the applied forces.

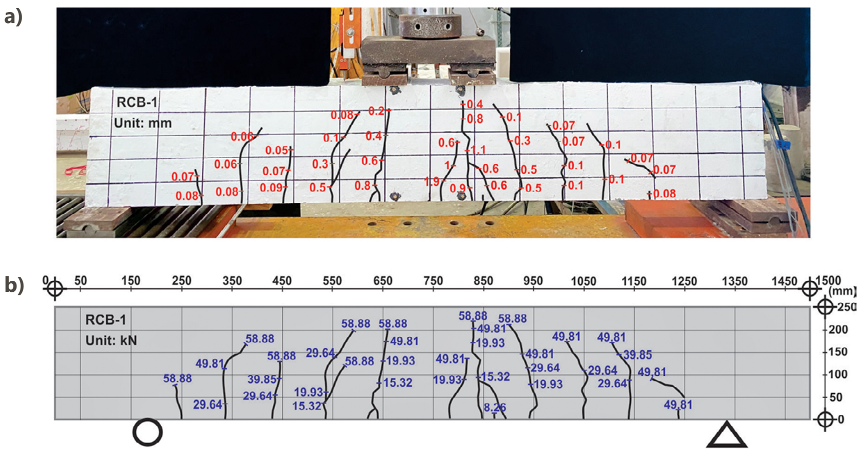

Figure 12. Crack propagation at the surface of RCB-1 during the loading phase: a – crack width; b – applied load

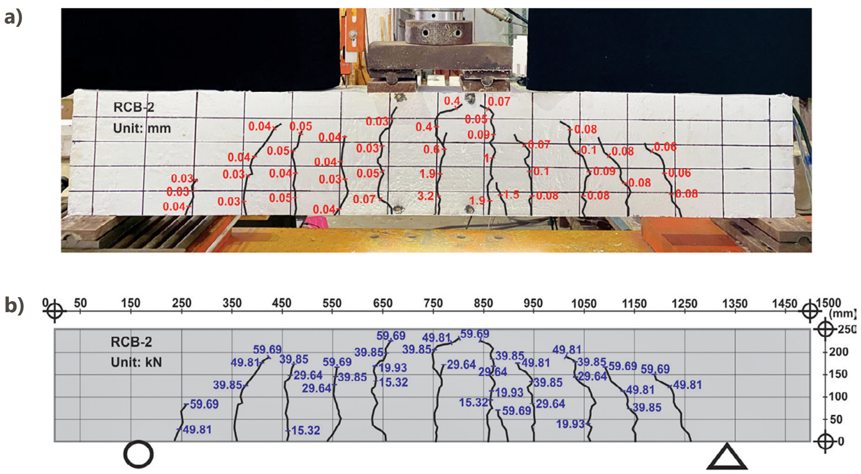

Figure 13. Crack propagation at the surface of RCB-2 during the loading phase: a – crack width; b – applied load

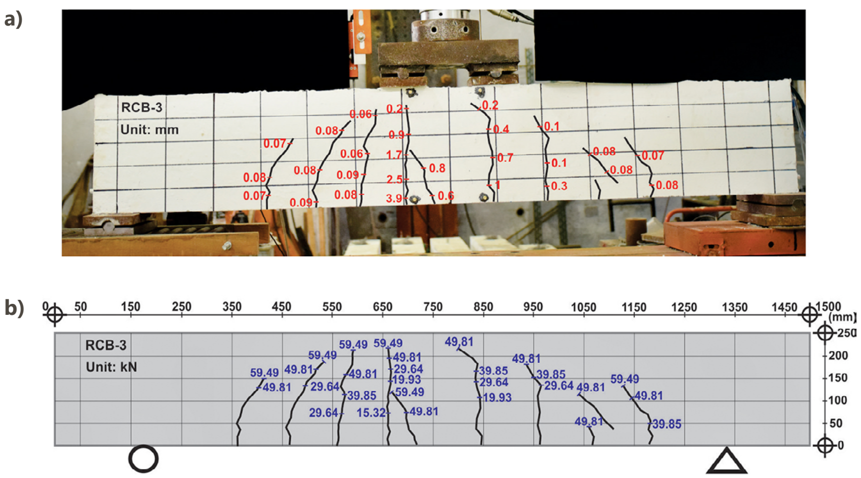

Figure 14. Crack propagation at the surface of RCB-3 during the loading phase: a – crack width; b – applied load

Table 2. Mechanical properties of RCB-1 during the loading phase

Load	Mid-span deflection, *d*	Rebar strain, e_S		Concrete strain, e_C		Crack width
		Compression zone	Tension zone	Compression zone	Tension zone	
(kN)	(mm)					(mm)
8.26	0.939	0.00007	0.00021	0.0001	0.0001	0.06 to 1.9
15.32	1.522	0.00012	0.00063	0.0003	0.0005	
29.64	3.305	0.00013	0.00129	0.0005	0.0016	
49.81	7.085	0.00044	0.01479	0.0014	0.0094	
58.88	14.494	0.00124	0.01262	0.0026	0.0163	

Table 3. Mechanical properties of RCB-2 during the loading phase

Load	Mid-span deflection, *d*	Rebar strain, e_S		Concrete strain, e_C		Crack width
		Compression zone	Tension zone	Compression zone	Tension zone	
(kN)	(mm)					(mm)
8.26	1.016	0.00004	0.00007	0.0001	0.0001	0.03 to 3.3
15.32	1.595	0.00263	0.00179	0.0002	0.0005	
29.64	3.218	0.00248	0.00688	0.0006	0.0010	
49.81	7.044	0.00247	0.45447	0.0016	0.0060	
59.69	14.526	0.00124	0.01262	0.0026	0.0122	

Table 4. Mechanical properties of RCB-3 during the loading phase

Load	Mid-span deflection, *d*	Rebar strain, e_S		Concrete strain, e_C		Crack width
		Compression zone	Tension zone	Compression zone	Tension zone	
(kN)	(mm)					(mm)
8.26	0.566	0.00007	0.00004	0.0002	0.0001	0.06 *to* 3.9
15.32	1.166	0.00016	0.00368	0.0002	0.0003	
29.64	2.905	0.00030	0.00913	0.0006	0.0010	
49.81	6.760	0.00101	0.00277	0.0014	0.0048	
59.49	15.260	0.00274	0.00000	0.0032	0.0109	

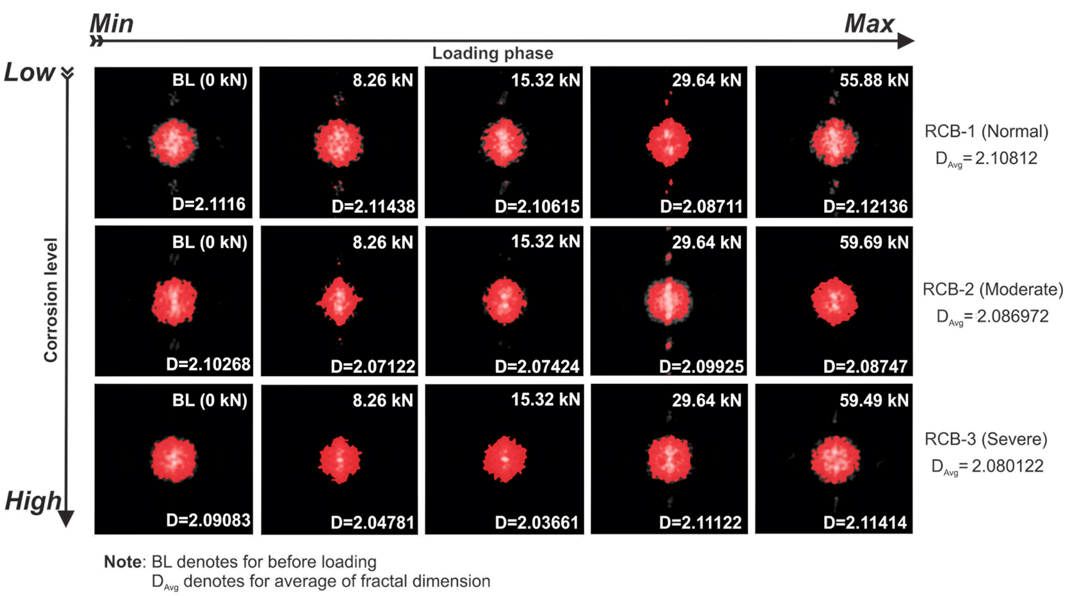

Figure 15. EM-wave images at each loading phase corresponding to their fractal dimension index

Subsequent to our initial analysis, we delved deeper into exploring the intricate relationship between the mechanical properties of reinforced concrete structures and the fractal dimension corresponding to distinct loading phases. To unravel this complex interplay, we generated a series of encoded images at each loading phase, as depicted in Figure 15. We explored the correlation between the fractal dimension of each specimen and their mechanical properties, as showed in Figure 16. Figure 16 presents the correlation between the fractal dimension, maximum deflection, and maximum crack width for the three RCB specimen under varying levels of corrosion. The result shows that as the corrosion level increases from normal (RCB-1) to moderate (RCB-2) to severe (RCB-3), the average of fractal dimension (D_{Avg}) decreases, indicating a reduction in structural strength. In contrast, both the maximum deflection and maximum crack width increase significantly, reflecting the deteriorating mechanical properties due to corrosion. These results collectively underscore the close connection between the encoded images of EM-wave's fractal dimension and the behavior of reinforced concrete structures. The fractal dimension is then used as indicator to labeled the image dataset for subsequent deep learning predictive model.

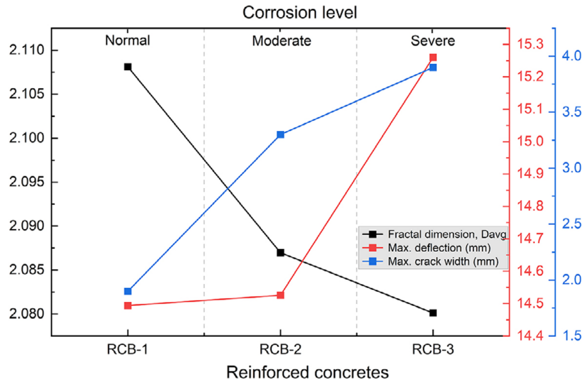

Figure 16. Correlation of fractal values with mechanical properties of RC structures

4.2. Predictive model performance evaluation

In the methodological exploration of fine-tuning our deep learning model, Table 5 succinctly encapsulates the hyperparameter search conducted to optimize model performance. The table presents a structured experimentation framework where each of the 10 experiments systematically varies key hyperparameters, specifically the learning rate and epoch size, while maintaining consistency in other parameters such as shear range, zoom range, dense layer count, and dropout rate.

The experiments are designed to evaluate the effects of different learning rates and training durations on model efficacy. Experiments 1 through 5 alternate the learning rate between 0.001 and 0.0001 while progressively increasing the epoch size from 16 to 64. This first set of tests is aimed at understanding the basic impacts of learning rate adjustments on short to moderate training cycles. Experiments 6 through 10 extend this exploration by maintaining learning rate between 0.001 and 0.0001 while further increasing the epoch sizes from 64 to a substantial 256, providing insights into the model's performance over longer training periods.

This systematic variation allows us to dissect the interplay between learning rate and training duration, crucial for identifying an optimal balance that maximizes accuracy without incurring unnecessary computational costs or overfitting. The shear range and zoom range are fixed at 0.2 and 0.5, respectively, ensuring that the model's responsiveness to input data augmentation remains constant and does not confound the effects of learning rate and epoch adjustments. The consistency in the dropout rate at 0.5 across all experiments is a strategic choice to mitigate any potential overfitting as the network complexity increases with more prolonged training. Similarly, keeping the number of dense layers fixed ensures that any observed changes in performance are primarily attributable to the varied learning rates and epoch sizes, rather than architectural modifications.

Table 6 shows the performance metrics of our CNN model over 10 training epochs, providing insights into the model's learning efficacy and generalization capabilities. The table shows a consistent increase in training accuracy, from 0.865538 in the first epoch to 0.889442 by the tenth epoch, indicating a steady improvement in the model's ability to learn from the training dataset. Correspondingly, the training loss decreases from 0.30625 to 0.299674, which further substantiates the model's growing proficiency in minimizing prediction errors as training progresses.

Table 5. Hyperparameter search for fine-tuning model performance

No	Shear range	Zoom range	Learning rate	Batch size	Epoch	Dense layer	Dropout
1	0.2	0.5	0.001	16	10	3	0.5
2	0.2	0.5	0.0001	16	10	3	0.5
3	0.2	0.5	0.001	32	15	3	0.5
4	0.2	0.5	0.0001	32	15	3	0.5
5	0.2	0.5	0.001	64	10	3	0.5
6	0.2	0.5	0.0001	64	10	3	0.5
7	0.2	0.5	0.001	128	15	3	0.5
8	0.2	0.5	0.0001	128	15	3	0.5
9	0.2	0.5	0.001	256	10	3	0.5
10	0.2	0.5	0.0001	256	10	3	0.5

Table 6. Model metrics performance

Epoch	Training accuracy	Validation accuracy	Training loss	Validation loss
1	0.865538	0.894531	0.30625	0.257315
2	0.87251	0.896484	0.29696	0.239555
3	0.871514	0.888672	0.284058	0.346328
4	0.868526	0.902344	0.313598	0.266706
5	0.884462	0.908203	0.271442	0.31352
6	0.893426	0.904297	0.266156	0.314864
7	0.888446	0.904297	0.27976	0.218981
8	0.896414	0.892578	0.26823	0.217366
9	0.875	0.892578	0.305072	0.300236
10	0.889442	0.90625	0.299674	0.214367

Interestingly, the validation accuracy and loss, which are critical indicators of the model's ability to generalize to new, unseen data, exhibit a slightly different pattern. While validation accuracy begins at 0.894531 and peaks at 0.908203 during the fifth epoch, it shows minor fluctuations but closes at a high of 0.90625 in the final epoch. Validation loss mirrors this pattern to some extent, starting at 0.257315 and ending at its lowest point of 0.214367 in the tenth epoch. These trends are indicative of the model's robustness, as the validation metrics do not diverge negatively from the training metrics, thereby suggesting that overfitting is minimal. The close tracking of training and validation accuracy alongside the reduction in losses across both domains suggests that the model is well-calibrated and continuing to learn effectively up to the tenth epoch. This is further evidenced by the gradual convergence of accuracy and loss, highlighting efficient learning without overfitting.

The confusion matrices generated by our CNN model were scrutinized to determine the model's effectiveness in differentiating between normal and reduced strength conditions within reinforced concrete structures. To gauge the classification efficacy of the model, we employed four critical performance indicators: precision, recall, accuracy, and the F1-score.

Precision is defined as the proportion of true positive predictions (TP) relative to the total number of positive predictions made, including both true positives and false positives (FP). This metric illustrates the model's accuracy in identifying only relevant instances as positive. Recall, on the other hand, measures the model's capability to correctly identify all actual positives from the dataset, accounting for both true positives and false negatives (FN), thereby highlighting the model's sensitivity to detecting positive instances. Accuracy provides a measure of the overall correctness of the model by considering both true positives and true negatives (TN). Additionally, the F1-score serves as the harmonic mean between precision and recall, offering a balanced measure of the model's performance across these two metrics. These evaluations are derived from the following mathematical formulas:

$$\text{Precision} = \frac{\text{TP}}{\text{TP}+\text{FP}}; \quad (3)$$

$$\text{Recall} = \frac{\text{TP}}{\text{TP}+\text{FN}}; \quad (4)$$

$$\text{Accuracy} = \frac{\text{TP}+\text{TN}}{\text{TP}+\text{FP}+\text{TN}+\text{FN}}; \quad (5)$$

$$\text{F1}-\text{score} = 2\times\frac{\text{Precision}\times\text{Recall}}{\text{Precision}+\text{Recall}}. \quad (6)$$

The following results is the optimal model that we set with the learning rate, batch size, and epoch, are 0.001, 128, and 10, respectively. The model demonstrated a robust ability to classify both conditions with considerable accuracy. Specifically, it correctly identified 169 instances as normal and 320 instances as reduced strength. However, the model also exhibited some limitations, with 23 false negatives for the normal class and 28 false positives for the reduced strength class. The result of the model confusion matrix can be seen in Figure 17.

The true positives for normal and reduced strength suggest that the model is generally effective at recognizing and categorizing the correct conditions. However, the presence of false negatives and positives indicates areas for improvement. False negatives, where the model incorrectly labeled normal conditions as reduced strength, could lead to unnecessary interventions, potentially increasing operational of maintenance costs for practical application. Conversely, false positives, where reduced strength conditions are misclassified as normal, pose a significant risk as they may lead to the oversight of critical structural weaknesses.

These discrepancies underscore the need for further model refinement to enhance its precision and recall, particularly to minimize risks in practical applications. Optimizing the model could involve more sophisticated data preprocessing, feature selection, or exploring more complex model architectures. Our analysis not only validates the model's current utility in structural health monitoring but also highlights the critical pathway for future research aimed at improving the reliability and safety of infrastructure assessments.

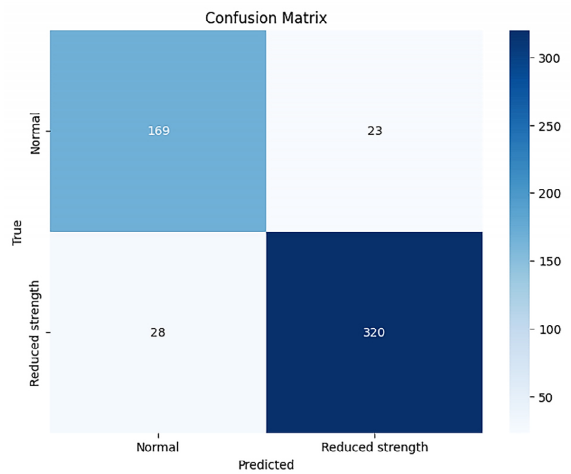

Figure 17. Confusion matrix

In subsequent analysis, we investigate the classification performance of our deep learning model, which was developed to discern between normal and reduced strength conditions in reinforced concrete structures. Table 7 systematically reports on three critical evaluation metrics – precision, recall, and F1-score – alongside the overall model accuracy, providing a comprehensive insight into the model's effectiveness. For the classification of normal conditions, the model achieved a precision of 0.86. This precision metric indicates that 86% of the instances classified as normal were correct, reflecting a high level of accuracy in identifying structures that do not exhibit signs of degradation. The recall of 0.88 for the normal condition suggests that the model successfully identified 88% of all actual normal cases, illustrating its ability to capture the majority of non-problematic instances without significant omissions. The F1-score, at 0.87, indicates a strong balance between precision and recall, signifying that the model performs reliably in scenarios where the strength of the structure is not compromised.

In the more critical of reduced strength classification, the model displayed even higher efficacy, with a precision of 0.93. This demonstrates that when the model predicts a reduced strength condition, there is a 93% likelihood that such a prediction is accurate, which is crucial for safety-critical applications where the cost of a false positive can be significant. The recall for reduced strength stood at 0.92, indicating that 92% of all actual deteriorated conditions were correctly identified by the model. This high recall is particularly important in preventive maintenance and safety assessments, where failing to detect an actual case of structural weakening could lead to catastrophic outcomes. The F1-score of 0.93 reinforces the model's robustness, showing a superior capability to balance precision and recall in detecting these crucial conditions. The overall accuracy of the model is reported at 0.91, which encapsulates its general efficiency across both classes. This high level of accuracy indicates that the model is highly capable of distinguishing between normal and compromised structural conditions, suggesting the model prediction could be effectively implemented in real-world monitoring systems for early detection of potential failures in reinforced concrete structures. The detail of classification result can be seen in Table 7.

We present a comprehensive analysis of our classification model performance through the Precision-Recall curve (as shown in Figure 18), which showcases a notably high area under the curve (AUC) of 0.983. This curve is crucial in illustrating the model's precision and recall balance across varying thresholds, providing our audience with a deep understanding of its predictive accuracy in classifying the conditions of reinforced concrete structures as either normal or reduced strength.

The curve begins with an exceptionally high precision close to 1.00, which remains above 0.95 across most of the recall spectrum. This robust capacity of the model to accurately identify true reduced strength conditions while maintaining a low rate of false positives is a testament to its reliability, which is crucial for applications where the integrity of structural assessments is paramount. However, as the recall extends towards 1.00, a slight but gradual decrease in precision is observed, a common characteristic in classification tasks, where increasing the sensitivity to capture all positive cases typically leads to accepting more false positives.

Table 7. Classification result

Classification	Precision	Recall	F1-score
Normal	0.86	0.88	0.87
Reduced strength	0.93	0.92	0.93
Accuracy	0.91		

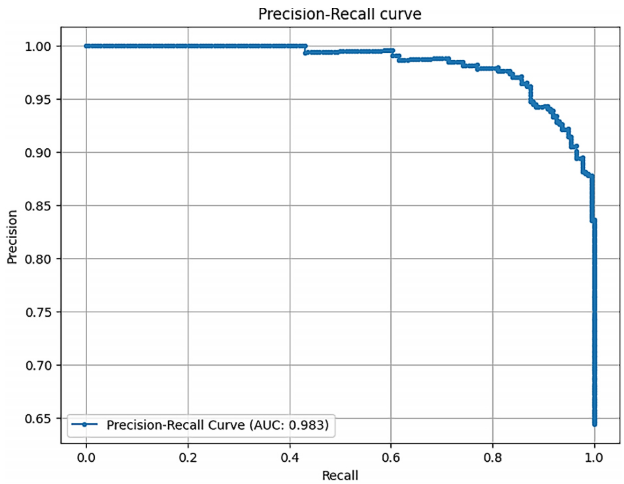

Figure 18. Precision-recall curve

Significantly, there is a sharp decline in precision at the high recall end, where precision decrease to around 0.65. This drop underscores the model's limitations where maximizing recall to capture every potential reduced strength instance increases the false positive rate. This aspect of the model's performance highlights the inherent trade-off between recall and precision that needs careful consideration, especially in safety-critical applications like structural health monitoring.

This analysis confirms the model's effectiveness in detecting critical conditions with high precision and emphasizes the practical implications of selecting an operational point on the curve. Depending on the threshold chosen, one can balance the need to minimize missed detections of compromised structures against the cost implications of false alarms. By adjusting the threshold according to specific risk tolerance and operational requirements, the model can be tailored to optimize both safety outcomes and operational efficiency in real-world applications.

5. Conclusions and future work

This study presents a pioneering framework for evaluating the structural performance of reinforced concrete structures by integrating electromagnetic wave data obtained via RFID technology with advanced image processing and deep learning technique. Our interdisciplinary approach successfully combines RFID technology, 2D Fourier transform, fractal dimension analysis, and convolutional neural networks into a cohesive and innovative method for structural health monitoring. The theoretical contributions of this research include the advancement of non-destructive testing methods through the use of EM waves for assessing structural integrity and the novel application of CNNs for classifying structural conditions based on EM wave images. The integration of fractal dimension analysis provides a quantitative measure of image complexity that correlates with structural integrity, enhancing the predictive capabilities of our model. Practically, this framework offers a cost-effective and low-maintenance solution for monitoring of RC structures, enabling early detection of potential failures and facilitating timely preventive maintenance. Its high accuracy (0.91) and F1-score (0.93) ensure efficient resource utilization, minimizing false positives and negatives, which is critical for safety and operational efficiency. Moreover, the framework's scalability and adaptability make it suitable for diverse applications, from small-scale infrastructure projects to large-scale urban development, providing a robust tool for engineers and maintenance professionals.

While our study has demonstrated significant promise, several areas for future research can further enhance the framework's capabilities. Enhanced feature engineering will involve exploring additional image processing techniques and features extracted from EM wave data to improve model accuracy and robustness, as well as integrating other types of sensors and data sources for a more comprehensive assessment of structural health. Algorithm optimization is another key area, where optimizing the CNN architecture and training process, including experimenting with different network architectures, hyperparameters, and training strategies, will be essential. Implementing advanced machine learning techniques such as ensemble learning and transfer learning can further enhance predictive capabilities. Expanding the dataset by including more varied structural conditions and larger sample sizes will improve model generalization and reliability. Additionally, conducting long-term monitoring studies will validate the framework's performance over extended periods and under different environmental conditions. Finally, field trials on actual RC structures will evaluate the framework's effectiveness in real-world scenarios, providing valuable insights into practical challenges and potential improvements. Collaborations with industry partners to integrate the framework into existing structural health monitoring systems will facilitate broader adoption and practical impact. Addressing these areas in future research will build upon the foundational contributions of this study, advancing the state-of-the-art in structural health monitoring and contributing to safer and more efficient infrastructure management.

Acknowledgements

The authors would like to thank the National Science and Technology Council, Taiwan, R.O.C, for financially supporting this research (ID: MOST 107-2218-E-008-016-MY2, MOST 109-2221-E-008-003-MY3).

Funding

This work was supported by the National Science and Technology Council, Taiwan, R.O.C under Grant numbers MOST 107-2218-E-008-016-MY2 and MOST 109-2221-E-008-003-MY3.

Author contributions

AP was responsible for Investigation, Data curation, Visualization, Writing-Original draft preparation. BXH was responsible for Investigation, Software, and Validation. THL was responsible for Conceptualization, Methodology, Writing-Reviewing and Editing, Supervision.

Disclosure statement

The authors declare that they have no known competing financial interests or personal relationships that could have appeared to influence the work reported in this paper.

References

ASTM International. (2021). *Standard guide for examination and evaluation of pitting corrosion* (G 46-21).

Atha, D. J., & Jahanshahi, M. R. (2018). Evaluation of deep learning approaches based on convolutional neural networks for corrosion detection. *Structural Health Monitoring*, *17*(5), 1110–1128. https://doi.org/10.1177/1475921717737051

Azad, A. K., Ahmad, S., & Azher, S. A. (2007). Residual strength of corrosion-damaged reinforced concrete beams. *ACI materials Journal*, *104*(1), Article 40. https://doi.org/10.14359/18493

Ballim, Y., Reid, J. C., & Kemp, A. R. (2001). Deflection of RC beams under simultaneous load and steel corrosion. *Magazine of Concrete Research*, *53*(3), 171–181. https://doi.org/10.1680/macr.55.4.405.37588

Ballim, Y., & Reid, J. C. (2003). Reinforcement corrosion and the deflection of RC beams – an experimental critique of current test methods. *Cement and Concrete Composites*, *25*(6), 625–632. https://doi.org/10.1016/S0958-9465(02)00076-8

Bartholmai, M., Johann, S., Kammermeier, M., Müller, M., & Strangfeld, C. (2016, October). Transmission characteristics of RFID sensor systems embedded in concrete. In *2016 IEEE Sensors*. IEEE. https://doi.org/10.1109/ICSENS.2016.7808920

Behnia, A., Chai, H. K., Yorikawa, M., Momoki, S., Terazawa, M., & Shiotani, T. (2014). Integrated non-destructive assessment of concrete structures under flexure by acoustic emission and travel time tomography. *Construction and Building Materials*, *67*, 202–215. https://doi.org/10.1016/j.conbuildmat.2014.05.011

Campione, G., Cannella, F., & Cavaleri, L. (2017). Shear and flexural strength prediction of corroded RC beams. *Construction and Building Materials*, *149*, 395–405. https://doi.org/10.1016/j.conbuildmat.2017.05.125

Cavaleri, L., Barkhordari, M. S., Repapis, C. C., Armaghani, D. J., Ulrikh, D. V., & Asteris, P. G. (2022). Convolution-based ensemble learning algorithms to estimate the bond strength of the corroded reinforced concrete. *Construction and Building Materials*, *359*, Article 129504. https://doi.org/10.1016/j.conbuildmat.2022.129504

Chalioris, C. E., Kytinou, V. K., Voutetaki, M. E., & Karayannis, C. G. (2021). Flexural damage diagnosis in reinforced concrete beams using a wireless admittance monitoring system – Tests and finite element analysis. *Sensors*, *21*(3), Article 679. https://doi.org/10.3390/s21030679

Cha, Y.-J., Choi, W., & Büyüköztürk, O. (2017). Deep learning-based crack detection using convolutional neural networks. *Computer-Aided Civil and Infrastructure Engineering*, *32*(5), 361–378. https://doi.org/10.1111/mice.12263

Chiba, H., & Miyazaki, Y. (1998). Reflection and transmission characteristics of radio waves at a building site due to reinforced concrete slabs. *Electronics and Communications in Japan* (*Part I*: *Communications*), *81*(8), 68–80. https://doi.org/10.1002/(SICI)1520-6424(199808)81:8%3C68::AID-ECJA8%3E3.0.CO;2-#

Coronelli, D., & Gambarova, P. (2004). Structural assessment of corroded reinforced concrete beams: Modeling guidelines. *Journal of Structural Engineering*, *130*(8), 1214–1224. https://doi.org/10.1061/(ASCE)0733-9445(2004)130:8(1214)

Ramesht, M. H. (1995). Effect of corrosion on flexural behavior of ferrocement. *Journal of Ferrocement*, *25*(2), 105–113.

Draudvilienė, L., Meškuotienė, A., Raišutis, R., Tumšys, O., & Surgautė, L. (2022). Accuracy assessment of the 2D-FFT method based on peak detection of the spectrum magnitude at the particular frequencies using the lamb wave signals. *Sensors*, *22*(18), Article 6750. https://doi.org/10.3390/s22186750

Dogan, G., Arslan, M. H., & Ilki, A. (2023). Detection of damages caused by earthquake and reinforcement corrosion in RC buildings with deep transfer learning. *Engineering Structures*, *279*, Article 115629. https://doi.org/10.1016/j.engstruct.2023.115629

Du, Y., Clark, L. A., & Chan, A. H. (2007). Impact of reinforcement corrosion on ductile behavior of reinforced concrete beams. *ACI Structural Journal*, *104*(3), Article 285. https://doi.org/10.14359/18618

El Maaddawy, T., Soudki, K., & Topper, T. (2005). Long-term performance of corrosion-damaged reinforced concrete beams. *ACI Structural Journal*, *102*(5), Article 649. https://doi.org/10.14359/14660

Fan, L., & Shi, X. (2022). Techniques of corrosion monitoring of steel rebar in reinforced concrete structures: A review. *Structural Health Monitoring*, *21*(4), 1879–1905. https://doi.org/10.1177/14759217211030911

Fernandez, I., Herrador, M. F., Marí, A. R., & Bairán, J. M. (2018). Ultimate capacity of corroded statically indeterminate reinforced concrete members. *International Journal of Concrete Structures and Materials*, *12*(1), Article 75. https://doi.org/10.1186/s40069-018-0297-9

Ferreira, P. M., Machado, M. A., Carvalho, M. S., & Vidal, C. (2022). Embedded sensors for structural health monitoring: methodologies and applications review. *Sensors*, *22*(21), Article 8320. https://doi.org/10.3390/s22218320

Gonzalez, R. C., & Woods, R. E. (2018). *Digital image processing* (4th ed.). Pearson.

Halabe, U. B., Maser, K., & Kausel, E. (1989). *Propagation characteristics of electromagnetic waves in concrete*. US Army Research Office.

Jiang, S., & Georgakopoulos, S. V. (2011, April). Optimum wireless power transmission through reinforced concrete structure. In *2011 IEEE International Conference on RFID* (pp. 50–56). IEEE. https://doi.org/10.1109/RFID.2011.5764636

Jiang, S., Georgakopoulos, S. V., & Jonah, O. (2012, July). Power transmission for sensors embedded in reinforced concrete structures. In *Proceedings of the 2012 IEEE International Symposium on Antennas and Propagation*. IEEE. https://doi.org/10.1109/APS.2012.6348425

Jnaid, F., & Aboutaha, R. S. (2016). Residual flexural strength of corroded reinforced concrete beams. *Engineering Structures*, *119*, 198–216. https://doi.org/10.1016/j.engstruct.2016.04.018

Laxman, K. C., Tabassum, N., Ai, L., Cole, C., & Ziehl, P. (2023). Automated crack detection and crack depth prediction for reinforced concrete structures using deep learning. *Construction and Building Materials*, *370*, Article 130709. https://doi.org/10.1016/j.conbuildmat.2023.130709

Li, Z., Jin, Z., Wang, P., & Zhao, T. (2021). Corrosion mechanism of reinforced bars inside concrete and relevant monitoring or detection apparatus: A review. *Construction and Building Materials*, *279*, Article 122432. https://doi.org/10.1016/j.conbuildmat.2021.122432

Li, Q., Dong, Z., He, Q., Fu, C., & Jin, X. (2022). Effects of reinforcement corrosion and sustained load on mechanical behavior of reinforced concrete columns. *Materials*, *15*(10), Article 3590. https://doi.org/10.3390/ma15103590

Lin, T. H., Putranto, A., & Wang, Y. T. (2021). Smart sensor tags for seepage sensing protected by 3D-printed case for embedding in concrete structures. *Construction and Building Materials*, *284*, Article 122784. https://doi.org/10.1016/j.conbuildmat.2021.122784

Lin, T. H., Putranto, A., Wang, Y. T, Yang, Q. H, Wu, R. J., Liu, C. H., Lin, C. K., & Chavali, M. (2022). Enhancing smart sensor tag sensing performance-based on modified plasma-assisted electrochemical exfoliated graphite nanosheet. *Polymers*, *14*(23), Article 5067. https://doi.org/10.3390/polym14235067

Lin, T. H., Chang, C. T., & Putranto, A (2024a). Real-time hollow defect detection in tiles using on-device tiny machine learning. *Measurement Science and Technology*, *35*(5), Article 056006. https://doi.org/10.1088/1361-6501/ad2665

Lin, T. H., Chang, C. T., Zhuang, T. H., & Putranto, A (2024b). Tiny machine learning empowers climbing inspection robots for real-time multiobject bolt-defect detection. *Engineering Applications of Artificial Intelligence*, *133*, Article 108618. https://doi.org/10.1016/j.engappai.2024.108618

Mehta, P. K., & Monteiro, P. J. (2014). *Concrete*: *microstructure*, *properties*, *and materials*. McGraw-Hill Education.

Meng, Z., & Li, Z. (2016). RFID tag as a sensor-a review on the innovative designs and applications. *Measurement Science Review*, *16*(6), Article 305. https://doi.org/10.1515/msr-2016-0039

Nguyen, N.-M., & Chou, J.-S. (2024). Forecasting mechanical properties of steel structures through dynamic metaheuristic optimization for adaptive machine learning. *Journal of Civil Engineering and Management*, *30*(5), 414–436. https://doi.org/10.3846/jcem.2024.21356

Obunguta, F., Matsushima, K., & Susaki, J. (2024). Probabilistic management of pavement defects with image processing techniques. *Journal of Civil Engineering and Management*, *30*(2), 114–132. https://doi.org/10.3846/jcem.2024.20401

Putranto, A., Lin, T. H., & Huang, B. X. (2023). Investigating the effect of corrosion in reinforced concrete structure with novel encoded electromagnetic wave imaging technique. In *Taiwan Concrete Institute 2023 Conference on Concrete Engineering*, Taipei, Taiwan. https://doi.org/10.5281/zenodo.11125725

Putranto, A., Lin, T. H., & Huang, B. X. (2024). Deep learning-integrated electromagnetic imaging for evaluating reinforced concrete structures in water-contact scenarios. *Automation in Construction*, *164*, Article 105459. https://doi.org/10.1016/j.autcon.2024.105459

Rucka, M., & Wilde, K. (2015). Ultrasound monitoring for evaluation of damage in reinforced concrete. *Bulletin of the Polish Academy of Sciences*: *Technical Sciences*, *63*(1), 65–75. https://doi.org/10.1515/bpasts-2015-0008

Senin, S. F., Hamid, R., Ahmad, J., Rosli, M. I. F., Yusuff, A., Rohim, R., Ghani, K. D. A., & Noor, S. M. (2019). Damage detection of artificial corroded rebars and quantification using non-destructive methods on reinforced concrete structure. *Journal of Physics*: *Conference Series*, *1349*, Article 012044. https://doi.org/10.1088/1742-6596/1349/1/012044

Strangfeld, C., Johann, S., & Bartholmai, M. (2019). Smart RFID sensors embedded in building structures for early damage detection and long-term monitoring. *Sensors*, *19*(24), Article 5514. https://doi.org/10.3390/s19245514

Taheri, S. (2019). A review on five key sensors for monitoring of concrete structures. *Construction and Building Materials*, *204*, 492–509. https://doi.org/10.1016/j.conbuildmat.2019.01.172

Taiwan Transportation Safety Board. (2023). *Final report released on Nanfangao sea-crossing bridge collapse*. https://www.ttsb.gov.tw/english/16051/16113/16114/28249/post

Tao, L., & Xue, X. (2024). An improved random forest model to predict bond strength of FRP-to-concrete. *Journal of Civil Engineering and Management*, *30*(6), 520–535. https://doi.org/10.3846/jcem.2024.21636

Val, D. V. (2007). Deterioration of strength of RC beams due to corrosion and its influence on beam reliability. *Journal of Structural Engineering*, *133*(9), 1297–1306. https://doi.org/10.1061/(ASCE)0733-9445(2007)133:9(1297)

Yeum, C. M., & Dyke, S. J. (2015). Vision-based automated crack detection for bridge inspection. *Computer-Aided Civil and Infrastructure Engineering*, *30*(10), 759–770. https://doi.org/10.1111/mice.12141

Zhang, J., Tian, G. Y., Marindra, A. M., Sunny, A. I., & Zhao, A. B. (2017). A review of passive RFID tag antenna-based sensors and systems for structural health monitoring applications. *Sensors*, *17*(2), Article 265. https://doi.org/10.3390/s17020265

Zhang, W., Zhang, H., Gu, X., & Liu, W. (2018). Structural behavior of corroded reinforced concrete beams under sustained loading. *Construction and Building Materials*, *174*, 675–683. https://doi.org/10.1016/j.conbuildmat.2018.04.145

Zhang, J., Cao, Y., Xia, L., Zhang, D., Xu, W., & Liu, Y. (2023). Intelligent prediction of the frost resistance of high-performance concrete: a machine learning method. *Journal of Civil Engineering and Management*, *29*(6), 516–529. https://doi.org/10.3846/jcem.2023.19226

Zhu, W., François, R., Coronelli, D., & Cleland, D. (2013). Effect of corrosion of reinforcement on the mechanical behaviour of highly corroded RC beams. *Engineering Structures*, *56*, 544–554. https://doi.org/10.1016/j.engstruct.2013.04.017

APPENDIX

Encoding raw data into image

Algorithm 1

Input: CSV file

Output: Encoded image of EM-wave

```
Import libraries (os, numpy, pandas, and PIL)
def create_image(type, weight, timing, scale, chunk_size):
  path = f”{type}/{weight}/{timing}”
print(f”start on data {path}”)
data = pd.DataFrame()
for i in range(1, 9):
    filename = f”./data/{path}/group{i}.csv”
    try:
        df = pd.read_csv(filename, header=None, names=[
              ‘node’, ‘unamed’, ‘rssi_label’, ‘rssi’, ‘freq_label’, ‘freq’, ‘ensor_label’, ‘ensor’])
        data[i] = df[‘freq’]
      except FileNotFoundError:
        print(f”File not found: {filename}”)
        continue
data = data.fillna(0).astype(int)
min_val = 902750
max_val = 927250
img_width = 8
img_height = chunk_size
# Data Normalization
 norm_data = (data - min_val) / (max_val - min_val)
# Convert data to range 0-255
norm_data_255 = np.clip(norm_data * 255, 0, 255).astype(‘uint8’)
 data = norm_data_255
sisa = data.shape[0] % chunk_size
 if sisa!= 0:
    padding = pd.DataFrame(
        np.zeros((chunk_size - sisa, data.shape[1])), columns=data.columns)
     data = pd.concat([data, padding])
 chunks = [data.iloc[i:i+chunk_size, :] for i in range(0, data.shape[0], chunk_size)]
for i, chunk in enumerate(chunks):
    imgs_data = []
    img = Image.new(‘L’, (img_width*scale, img_height*scale), color=0)
     df_array = chunk.values
     try:
        resize_img = np.repeat(np.repeat(df_array, scale, axis=0), scale, axis=1)
       img.putdata(resize_img.flatten().tolist())
       imgs_data.append(img)
   except KeyError:
        print(f”KeyError: {df_array}”)
        continue
  # Create Image
   combined_img = np.concatenate([np.array(img) for img in imgs_data], axis=1)
   combined_img_pil = Image.fromarray(combined_img)
   # Save Image
   img_path = f”dist/8x{chunk_size}/images_{scale}x/{path}”
   if not os.path.exists(img_path):
       os.makedirs(img_path)
   img_name = f”{i+1}.png”
   try:
     combined_img_pil.save(f”{img_path}/{img_name}”)
     print(f”saved image on {img_path}/{img_name}”)
 except PermissionError:
    print(f”PermissionError: Cannot save image to {img_path}/{img_name}”)
    continue
   print(f”data {path} finished \n\n”)
weights = [‘0.77tf’, ‘1.54tf’, ‘2tf’, ‘3tf’, ‘4tf’, ‘5tf’, ‘6tf’]
times = [‘90sec’, ‘180sec’, ‘300sec’]
RBS = [”RB1”, “RB2”, “RB3”]
scale = [10]
chunk_size = [8]
for c in chunk_size:
  for s in scale:
      for rb in RBS:
         for w in weights:
           for t in times:
             create_image(rb, w, t,s, c)
```